Journal of Power Sources 451 (2020) 227709

Contents lists available at ScienceDirect

Journal of Power Sources

journal homepage: www.elsevier.com/locate/jpowsour

Physical vapor deposition process for engineering Pt based oxygen reduction reaction catalysts on NbO_x templated carbon support

Chunchuan Xu [a,*], Jun Yang [a], Ershuai Liu [b], Qingying Jia [b], Gabriel M. Veith [c], Gokul Nair [c], Stephen DiPietro [d], Kai Sun [e], Jixin Chen [a], P. Pietrasz [a], Zijie Lu [a], Mark Jagner [a], Kerrie K. Gath [a], Sanjeev Mukerjee [b], James R. Waldecker [a]

[a] Ford Motor Company, Dearborn, MI, 48121, USA
[b] Department of Chemistry and Chemical Biology, Northeastern University, Boston, MA, 02115, USA
[c] Chemical Sciences Division, Oak Ridge National Laboratory, 1 Bethel Valley Rd, Oak Ridge, TN, 37830, USA
[d] Exothermics, Inc., 14 Columbia Drive, Amherst, NH, 03031, USA
[e] Department of Materials Science and Engineering, University of Michigan, 2300 Hayward Street, Ann Arbor, MI, 48109, USA

HIGHLIGHTS

- Physical vapor deposition was used to synthesize ORR catalysts for PEM fuel cells.
- The catalysts are composed of Pt or Pt-alloys on an NbO_x templated carbon support.
- The interaction of Pt and NbO_x increases catalyst durability and mass activity.
- Physical vapor deposition method reduces chemical pollution and production cost.

GRAPHICAL ABSTRACT

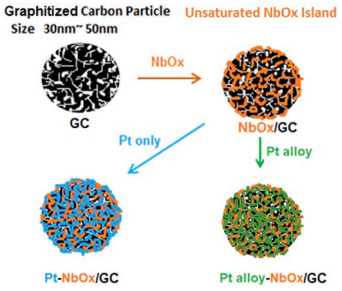

ARTICLE INFO

Keywords:
Oxygen reduction reaction (ORR) catalyst
Physical vapor deposition (PVD)
Arc plasma deposition (APD)
Non-stoichiometric niobium oxide (NbO_x)
X-ray absorption spectroscopy (XAS)
Membrane electrode assemble (MEA)
Accelerated stress test (AST)

ABSTRACT

Two physical vapor deposition (PVD) processes, magnetron sputtering (MS) and arc plasma deposition (APD), were investigated to prepare oxygen reduction reaction (ORR) catalysts for proton exchange membrane fuel cells (PEMFCs). The catalysts are composed of Pt or Pt alloy on a NbO_x decorated carbon support (NbO_x/C). The combination of these materials results in tunable structures and electronic properties and a commensurate increase in lifetime (>60% retention after 30,000 cycles) and initial MEA mass activities of over 300 $A g_{Pt}^{-1}$. *In situ* x-ray absorption spectroscopy (XAS) shows that there exists direct interaction between Pt and the O in the non-stoichiometric NbO_x in Pt on NbO_x/C catalyst. The introduction of Co leads to shortened Pt–Pt bond distance as confirmed by XAS, and a beneficial Pt on NbO_x strain effect. The relationship between Pt and NbO_x loading is discussed based on rotating disk electrode (RDE) data.

* Corresponding author.
E-mail address: cxu22@ford.com (C. Xu).

https://doi.org/10.1016/j.jpowsour.2020.227709
Received 27 September 2019; Received in revised form 1 January 2020; Accepted 2 January 2020
Available online 22 January 2020

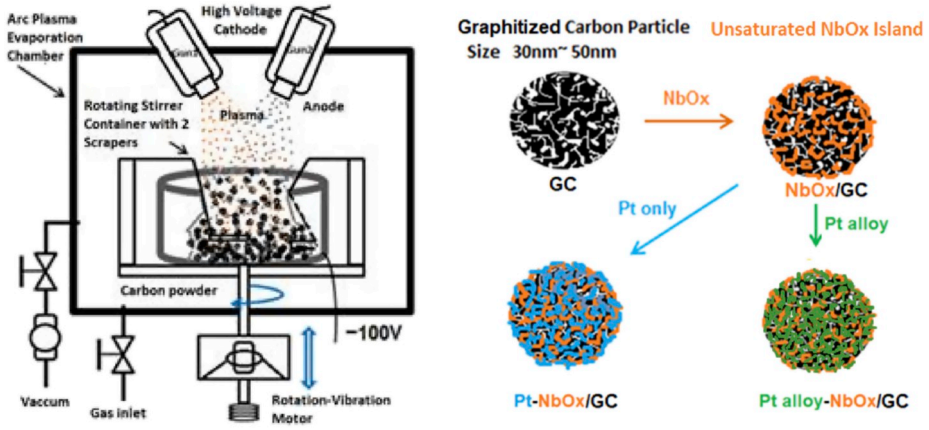

Fig. 1. APD deposition chamber with two plasma deposition guns (left). The schematic of Pt or Pt alloy-NbO_x/C catalysts synthesis process and structures (right).

1. Introduction

It has been well documented that the catalytic activity and stability of ORR catalysts for proton exchange membrane fuel cells need to be improved, with Pt loading reduced for a viable fuel cell vehicle application. Drawbacks of state-of-the-art wet-chemically processed dispersed platinum nanoparticles on carbon include carbon corrosion [1] and Pt dissolution [2] under operating conditions. These can lead to the loss of electrochemical active area and fuel cell performance degradation [3]. Many efforts have been devoted to improving catalyst durability, such as controlling the interactions between the support substrate and Pt, and engineering the specific crystal orientation of Pt nanoparticles, in combination with the selection of carbon nano-particles with various degrees of crystallinity [4,5]. One method to improve the catalyst has been through the incorporation of a conductive metal oxide support [6–8]. The system generally shows improved electrochemical stability and catalytic activity through Pt d-band modifications. NbO_x as a conductive metal oxide was also found to stabilize the Pt with enhanced activities and durability.

In this work, we implement a scalable physical vapor deposition (PVD) process to synthesize Pt-based ORR catalysts without the use of solutions. In this PVD processes high purity metal or metal oxide targets are atomized in a vacuum and the atomic species rain upon a substrate where they nucleate and form catalytic nanoparticles. A non-stoichiometric NbO_x layer was deposited on nano-sized carbon (or graphene, GR) powders as a novel catalyst support, followed by contiguous Pt deposition forming ORR catalysts for PEMFCs. Non-stoichiometric NbO_x is a niobium oxide with various degree of oxygen incorporation, where x is the degree of oxygen incorporation parameter between 1.0 and 2.5. For example, $x = 2.452$ represents $Nb_{22}O_{54}$. The fully saturated Nb_2O_5 is a non-conductive crystalline for electron transport and thus not a good candidate for catalyst support [9]. Janninck and Whitmore [10] studied the electrical conductivity of polymorphs NbO_x with more than 20 different stoichiometry deviations with x ranging from 2.428 to 2.499. They found the values widely varied between 10^{-3} and 10^{3} S/cm, which is a wide electrical conductivity range between semiconductor and conductor. As a support material, the low degree of oxygen incorporation in NbO_x corresponds to a high electrical conductivity, which is a critical condition for efficient catalyst system as reported by L. Zhang's group [11]. For the NbO_x stability, it is believed that NbO_x with the higher oxidation state has the higher stability in the electrochemical environment. The stability of NbO_x was also confirmed under RDE in our previous report [12]. In addition, Zhang's group also reported that Pt on NbO_2 functional layer was tested be well stable under RDE voltage cycling. On the other hand, the local (short-range) atomic order of NbO_x could facilitate the d-band interaction with Pt or Pt alloy to enhance the electro-catalytic activity via the Pt–O interaction [13]. In this study, Pt/NbO_x ORR catalysts were synthesized by MS and APD methods on disordered (KB), partially ordered carbon (AB), graphitic carbon (GC) nano-particles, and graphene (GR) flakes or graphene layers (GR-L), respectively. Their activity and durability were investigated in RDE and single cell tests.

2. Experimental methods

Catalyst synthesis: NbO_x and Pt were deposited onto carbon nanoparticles by a commercial APD system, which was modified from an Ulvac Inc. arc plasma deposition system by adding a ceramic heater underneath a rotatable stirring vessel, in order to control the sample temperature. Carbon or graphitic carbon nano-powders were loaded into the stirring vessel. The coating system layout is shown in Fig. 1a. The sample temperature was controlled at 350 °C at a vacuum level of 10^{-3} Pa. Target voltages were 150 V for NbO_x and 100 V for Pt, PtNi alloy or PtCo alloy target. A pure platinum target was used for Pt sputtering which could be changed to a Pt_3Ni alloy or Pt_3Co alloy target to perform alloy deposition. For examples, sample APD-1106 was made with 2500 and 40,000 pulses for NbO_x and Pt respectively at 300 °C. Sample APD-0110 was made with 3500 and 45,000 pulses for NbO_x and Pt respectively at 370 °C. All other samples were prepared by varying the number of pulses of NbO_x and Pt at 300 °C.

Oak Ridge National Laboratory (ORNL) [14–19] and Exothermics Inc. (EXO) have similar magnetron sputtering systems but at different scale. The magnetron sputtering system at ORNL can only produce small batch samples for research purposes. Magnetron sputtering systems at EXO can be used for batches of tens of grams to kilograms for commercial products, as shown in Supplementary Material. Sputtering deposition of NbO_x and Pt or Pt alloy catalyst onto candidate high surface area nano-sized carbon powder substrates was conducted in a vacuum chamber by scaled up carbon powder fluidization. DC or pulsed DC magnetron sputtering techniques were used with the intention to coat adherent, fine-grained deposits on carbon powder substrates for subsequent characterization. The sputtering chamber layout is shown in Supplementary Material.

The obtained NbO_x phases on nano-sized carbon particles were isolated NbO_x islands or partially connected NbO_x network, with the value of x (oxygen content) between 1 and 2.5. The loading of NbO_x is approximately 0.3–8.0 wt %. Ideally, when Pt or Pt alloy was deposited onto the pre-formed NbO_x, platinum nanoparticles settled between and/or on top of the NbO_x, creating a Pt network as reported in the previous paper [20]. A pair of plasma guns used in the APD system can deposit both NbO_x and Pt either simultaneously or in alternating fashion as schematically shown in Fig. 1 (left), with the intended deposition process and catalyst structure (right).

ORNL has two DC magnetron sputtering systems with different sized

chambers. The samples labeled "ORNL-###" were produced in the small chamber and those labeled with "ORNL-L###" were produced in the large chamber. Niobium deposition was from a pure Nb target for all samples in a 10:1 Ar:O_2 environment for 1.5 h at 150 W. The sputtered Nb atoms were oxidized during the sputtering process to form NbO_x. Pt deposition proceeded for all samples in Ar environment. Deposition times range from 1–6 h. Pt deposition power was 140 W for all samples except for ORNL-023 and ORNL-031, for which 70 W was used. The samples labeled "EXO-####" were produced by the large scale MS system of Exothermics Inc.

***Ex situ* microstructure and composition characterization**: Particle morphology and elemental analysis were performed with a Hitachi S−4800 field emission scanning electron microscope (SEM) combined with its energy dispersive X−ray spectroscopy (EDS) module, and a JEOL 2010 field emission gun (FEG) transmission electron microscope (TEM). XRF (X-ray fluorescence) was used to determine the catalyst compositions. Thin-layer specimens mounted onto 25 mm diameter cups were prepared by placing a sample of each powder and several drops of a water and ethanol mixture (with 3 deionized water to 1 ethanol volume ratio) between a 6.3 μm polypropylene support film and a gas permeable polypropylene film backing. A cotton tipped applicator was gently swept over the surface of the PPE support film to obtain a smooth, uniform thickness. The specimens were then dried at 60 °C for 30 min to remove the water/ethanol. The samples were analyzed under vacuum using a PANalytical PW2400 XRF Spectrometer and UniQuant5 quantitative analysis program. Various ratios of nominal 40% Pt/carbon black (Alfa Aesar 42204, certified 39.2% Pt), Nb_2O_5 powder (Alfa Aesar 10822, 99.9985%), and carbon black were used as reference materials to create a specialized UniQuant calibration to quantify Pt and Nb. The standard UniQuant calibration sensitivity factors based on single-element/single-compound reference materials were used to quantify all other elements.

***In situ* x-ray absorption spectroscopy (XAS)**: The electrode inks for the XAS electrodes were composed of 18.2 MΩ purity deionized water (Millipore), 2-propanol (HPLC-grade, Aldrich), 5 wt% EW1100 Nafion solution (Aldrich), and the synthesized catalyst powder. The composition was chosen to make a final electrode with a dry Nafion loading of 0.4 wt% (by weight percentage). The ink was hand-painted onto a Zoltek® carbon cloth and dried for 15 min in a 65 °C vacuum oven between coats. The final Pt and Nb gravimetric loadings were chosen to give 0.05 transmission spectra edge heights at the Pt L_3 and Nb K edges, respectively. The *in situ* XAS experiments were conducted at room temperature in a homemade spectra-electrochemical half-cell with continuously circulating 0.1 M $HClO_4$ electrolyte purged with N_2 or O_2. The catalyst-impregnated samples were conditioned in the electrolyte under vacuum for 45 min to remove surface oxides and contaminants before transferring to the half-cell (single-side coated membrane). Potentiostat control was maintained with an Autolab PGSTAT30 potentiostat/galvanostat (Metrohm USA, formerly Brinkman Instruments). The voltage cycling limits were 0.05–1.2 V (versus reversible hydrogen electrode) when collecting data at the Pt L_3 edge, and 0.05–1.5 V when collecting data at the Nb K edge. The electrode was potential cycled following each potential hold in order to clean the catalyst surface. Before each measurement, the cell was held for 5 min to reach a pseudo-steady state. Data collection was then performed at the chosen potentials held during anodic sweeps. All data were collected in the fluorescence mode at the beamlines of 8-ID and 6BM at the National Synchrotron Light Source II (NSLS-II) (Brookhaven National Laboratory, NY). All the experimental data were collected in conjunction with the appropriate reference foils to aid in energy alignment and normalization. The data were processed and fit using the IFEFFIT-based Athena [21] and Artemis [22] programs. Scans were calibrated, aligned and normalized with background removed using the IFEFFIT suite [23]. The χ(R) were modeled using single scattering paths calculated by FEFF6 [24]. The XANES (x-ray absorption near edge spectroscopy) analysis technique has been described in detail elsewhere [25–28].

RDE ink preparation and characterization: About 5 mg of the as-prepared catalyst was added to a 5 ml ink solution containing 20 vol % isopropanol (J.T. Baker, 99.9%), 79.6 vol % nano-pure water, and 0.4 vol % of 5 wt % EW1000 Nafion solution (Ion Power). The catalyst ink in a bottle was mixed under ultra-sonication for at least 1 h in ice water bath. A micropipette was used to deposit 8 μl of the mixed catalyst ink, which contained about 2.0 μg–4.0 μg Pt loading, in one drop on a 5 mm diameter gold tip (0.196 cm^2) facing up on a rotatable RDE shaft. The RDE shaft and tip were rotated at speeds between 100 rpm and 500 rpm, allowing the tip to dry overnight in air.

Electrochemical measurements: Thin-film rotating disc electrode (RDE) methodology (Pine Instruments, USA) was used to determine Pt electrochemical surface area (ECSA) and oxygen reduction reaction (ORR) activity in terms of area-specific (SA) and mass-specific (MA) activities. Cyclic voltammetry (CV) experiments were conducted for all prepared samples in Ar-saturated 0.1 M $HClO_4$ solution (GFS Chemicals Inc., OH, USA double distilled 70 wt% $HClO_4$) with rotation speed of 1600 rpm for positive-going potential sweeps between 0.05 V and 1.05 V versus reversible hydrogen electrode (RHE) at a constant temperature of 35 °C. The ECSA were derived by integrating the hydrogen desorption currents and using 210 μC cm^{-2} specific capacitance. ORR polarization curves of the prepared samples were recorded in an O_2-saturated solution with a scan rate of 20 mVs^{-1} [29]. RDE experiments were conducted with a gold tip working electrode, platinized-Pt mesh counter electrode, and H_2 gas/Pt mesh RHE reference electrode in a 35 °C thermostated three-compartment glass cell. The reference electrode was separated from the working electrode by means of a closed stopcock Luggin capillary to prevent hydrogen gas from leaking into the working electrode compartment. The counter electrode was separated from the working electrode cell by means of a glass frit. A Bio-Logic SP-150 potentiostat was used for data collection. The catalyst stability test was assessed by RDE under a square voltage wave between 0.1 V and 1.0 V with a duration of 3 s for each voltage level in an argon purged electrolyte. About 25,000 cycles has been applied RDE AST stability test from beginning-of-test (BOT) to end-of-test (EOT).

MEA test: A series of catalysts were investigated as the cathode catalyst layers in MEA testing. The catalyst inks were made by mixing the catalysts with the ionomer solution (Aquivion D83-06A, ionomer to carbon ratio = 0.6) and water-IPA solvent mixture, and sonicated in ice water for 1.5 h. The fresh inks were then spray-coated onto the Johnson Matthey (JM) half catalyst-coated membrane (CCM) by using a Sono-Tek ultrasonic spray system. The anode catalyst layer on the JM half-CCM had a platinum loading of 0.05 mg_{Pt} cm^{-2} and the membrane thickness was 18 μm. The cathode catalyst loading was controlled to be 0.10 mg_{Pt} cm^{-2}, which was confirmed by both the ICP and XRF measurements. The fabricated CCM was dried in vacuum oven at 80 °C for 24 h to completely evaporate the solvents. The SGL-29BC gas diffusion layer (GDL) Two 3-mil PTFE sheets were used as the gaskets for both the anode and cathode electrodes. The MEAs were loaded in Fuel Cell Technology 5 cm^2 single cell hardware and tested in the Scribner 850E fuel cell test stand under 80 °C, 150 kPa and 100% RH, following the US DOE fuel cell test protocol. The platinum accelerated stress tests (AST) were performed using a square wave voltage from 0.6 V to 0.95 V with a duration of 3 s for each voltage level according to US DOE MEA Pt AST protocol. Each test was run up to 30,000 cycles. The MEA's BOT and EOT performance metrics, such as polarization curves, mass activity, specific electrochemical surface areas, high frequency resistance (HFR) by AC impedance and H_2 crossover (H_2x-over), were recorded for analysis.

3. Results and discussion

As noted above the catalysts prepared by APD and MS are grown by physically different processes. The APD relies on the deposition of platinum nanoparticles while the MS relies on the deposition of atomic species and the nucleation of the atoms into small particles. As a result, the surface chemistry and surface interactions, which are not

Table 1
RDE ORR activity summary.

Sample[a]	Pt loading Wt. %	Roughness (cm^2/cm^2)	ECSA ($m^2g_{pt}^{-1}$)	SA (μAcm^{-2})	MA (Ag_{pt}^{-1})
Commercial Pt/GC	46.7%	9.37	56	297	165
PtNbF/GLC	2.4 nm (film)	1.10	22.9	2377	495
APD-Pt/GC	10%	1.19	28.4	749	213
APD-Pt/GR	10%	1.65	27.1	871	235
APD-PtNb/GC-a	13%	4.52	54.1	706	382
APD-PtNb/GC-b	20%	10.66	54.5	566	309
APD-PtNb/GC-c	10%	2.20	36.9	604	223
APD-PtNb/GR	10%	2.10	34.3	1003	345
APD-PtNb/GR-L	5%	2.27	33.6	1178	391

[a] This is earlier RDE data of APD catalysts tested before 2014.

understood, mediate the resulting particles and their stability. Compounding the challenge of understanding growth the deposition is in a "pulse" type configuration due to the non-periodic exposure of the fluidized support surface to the deposition flux as compared to the continuous growth of a thin film. Due to these differences the following sections are segregated based on MS and APD growth methods. Table 1 and Table 2 summarizes the samples made for this work and some of their electrochemical properties discussed later. The weight loading on all the samples was adjusted by varying the deposition time. Weight loading varied in a linear fashion depending on the time and total material in the fluidizing assembly.

3.1. Catalyst microstructure

Under the accelerating electric field in the PVD system, most of the sputtered platinum or platinum alloy nanoparticles fall onto the amorphous NbOx particles and/or the junction between the carbon surface and the deposited NbOx [12]. The interaction between Pt and NbOx particles can pin the Pt nanoparticles onto NbOx under high-energy deposition conditions to form a bond between NbOx and Pt or Pt alloy. For the ORNL-005 sample, which is 22.1% Pt and 1.86% NbOx by weight on GC, the platinum particles are isolated from each other with sizes of approximately 2 nm–5 nm, as shown in Fig. 2a, and a higher magnification STEM HAADF image in Fig. 2b. Agglomerated platinum particles were formed as shown in Fig. 2c for ORNL-011, where the Pt loading is 57.5% and the NbOx loading is 0.81% by weight. The STEM-EDS elemental map identified C, Pt, and Nb in Fig. 2d. Nb in green was evenly distributed on the graphitized carbon (Fig. 2e). Pt preferentially contacts with NbO_x, due likely to interactions between Pt and NbO_x, as it can be seen in Fig. 2e of the elemental trace EDS map of Nb and overlapped Pt in blue at the sample location in Fig. 2f.

ORNL-011 with 57.5% Pt loading shows that Pt nano-particles overlapped and agglomerated together (Fig. 2c). This configuration significantly reduced the effective catalyst surface area. This image explains why this sample had a relatively low RDE mass activity of 436 Ag_{pt}^{-1} and specific surface area of 39 $m^2g_{pt}^{-1}$ (Table 2). Since Pt nanoparticles were deposited onto the NbO_x/C top surface, the higher Pt loading led to greater likelihood that the Pt particles overlapped and formed a bigger particle, which led to a lower Pt specific surface area. The average particle size for both ORNL and EXO samples is around 2 nm, with distribution between 1 and 5 nm showed in Fig. 3. The Pt particle size was measured by TEM imaging method which counted about 100 separated Pt particles and avoided from the agglomerated Pt particle regions for a high Pt loading sample ORNL-023. It has been reported that for fuel cell application, the desired Pt particle size is between 2 and 5 nm to optimize both durability and ORR mass activity in wet-chemically processed Pt on carbon catalysts [30]. High uniformity of catalyst deposition on the powder substrates can be achieved by fine tuning PVD deposition conditions in our future work.

The comparisons of the stability between Pt-NbO_x/C catalysts and

Table 2
RDE data for APD, ORNL and Exothermics magnetron sputtered ORR catalysts.

Sample	Composition[a] (Wt.%)	MA (Ag_{Pt}^{-1})	SA (μAcm_{Pt}^{-2})	ECSA ($m^2g_{Pt}^{-1}$)	MA AST Retention Rate (%)
ORNL-095	0.0% Pt, 12.90% NbO_x, GC	N/A	N/A	N/A	N/A
ORNL-001	26.2% Pt, 5.90% NbO_x, GC	242	682	30	72
ORNL-002	35.7% Pt, 1.27% NbO_x, GC	292	489	35	83
ORNL-005	22.1% Pt, 1.83% NbO_x, GC	556	723	76	76
ORNL-010	47.3% Pt, 0.50% NbO_x, AB	591	1229	43	80
ORNL-011	57.5% Pt, 0.81% NbO_x, AB	436	1122	39	60
ORNL-015	36.2% Pt%, 0.0% NbOx, GC	350	828	40	64
ORNL-017	56.7% Pt%, 0.0% NbOx, GC	315	864	37	56
ORNL-022	23.1% Pt, 1.46% NbO_x, AB	513	1047	49	73
ORNL-023	60.8% Pt, 0.94% NbO_x, AB	477	1157	41	59
ORNL-024	46.1% Pt, 0.24% NbO_x, AB	529	1314	40	60
ORNL-031	62.2% Pt, 0.59% NbO_x, AB	456	1086	42	64
ORNL-L010	55.1% Pt, 1.41% NbO_x, AB	452	721	63	67
ORNL-L011	71.0% Pt, 0.73% NbO_x, AB	457	982	47	71
ORNL-L012	22.5% Pt, 1.19% NbO_x, AB	503	584	86	76
ORNL-L013	35.8% Pt, 0.61% NbO_x, AB	490	695	71	68
EXO-0731	0.0% Pt, 13.3% NbO_x, GC	N/A	N/A	N/A	N/A
EXO-0822	10.6% Pt, 6.3% NbO_x, GC	285	704	41	82
EXO-1117	19.7% Pt, 5.52% NbO_x, GC	420	806	50	79
EXO-0109	19.9% Pt, 1.75% NbO_x, KB	519	730	71	74
EXO-0302	21.5% Pt, 1.10% Co, 0.23% NbO_x, KB	653	926	67	63
EXO-0308	28.8% Pt, 1.54% Co, 0.5% NbO_x, KB	672	885	76	67
APD-1106	21.3% Pt, 2.39% NbO_x, GC	461	693	67	71
APD-0110	30.2% Pt, 3.75% NbO_x, AB	429	515	83	80
APD-0205	17.7% Pt, 1.58% Ni, 1.07% NbO_x, GC	539	504	107	N/A
APD-0302	13.9% Pt, 1.17% Co, 1.43% NbO_x, GC	449	634	71	N/A
APD-0415	22.5% Pt, 2.15% Co, 2.12% NbO_x, AB	607	883	69	N/A
COM-Pt/GC	46.7% Pt, GC	165	297	56	56

[a] The composition concentrations were examined by XRF. AB is acetylene black, KB is Ketjen black, GC is graphitized carbon. The two samples without Pt loading (0.0%) were used for XAS examination.

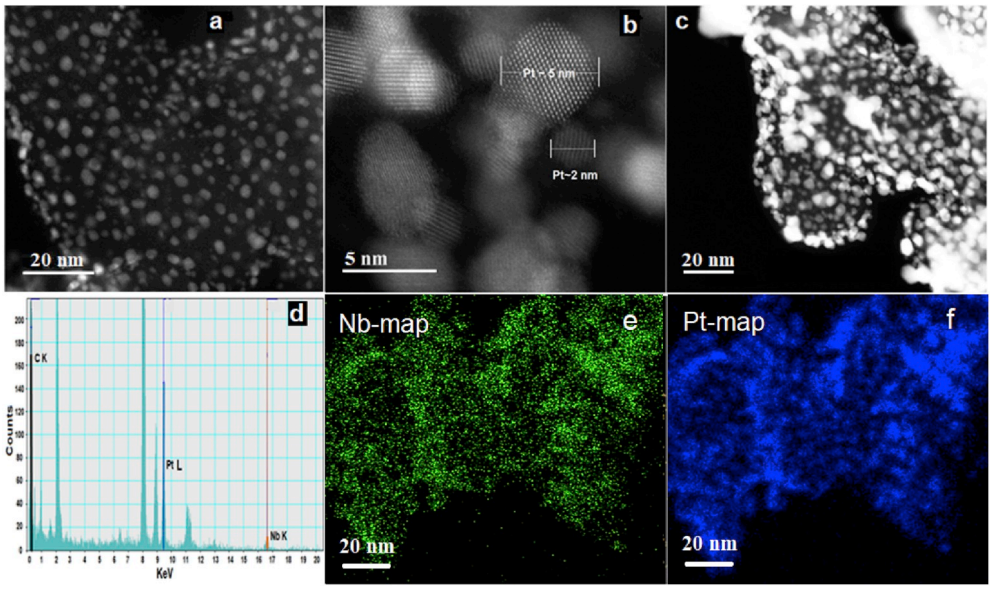

Fig. 2. (a) The top view of STEM HAADF images of ORNL-005 with 22.1 wt % Pt loading. (b) The higher magnification image of ORNL-005. (c) The image of Pt deposited on NbO_x/GC with 57.5% Pt loading for sample ORNL-011. (d) The EDS spectroscopy of the carbon, Pt and Nb composition of ORNL-005. (e) The EDS mapping of Nb of ORNL-005. (f) The EDS mapping of Pt of ORNL-005.

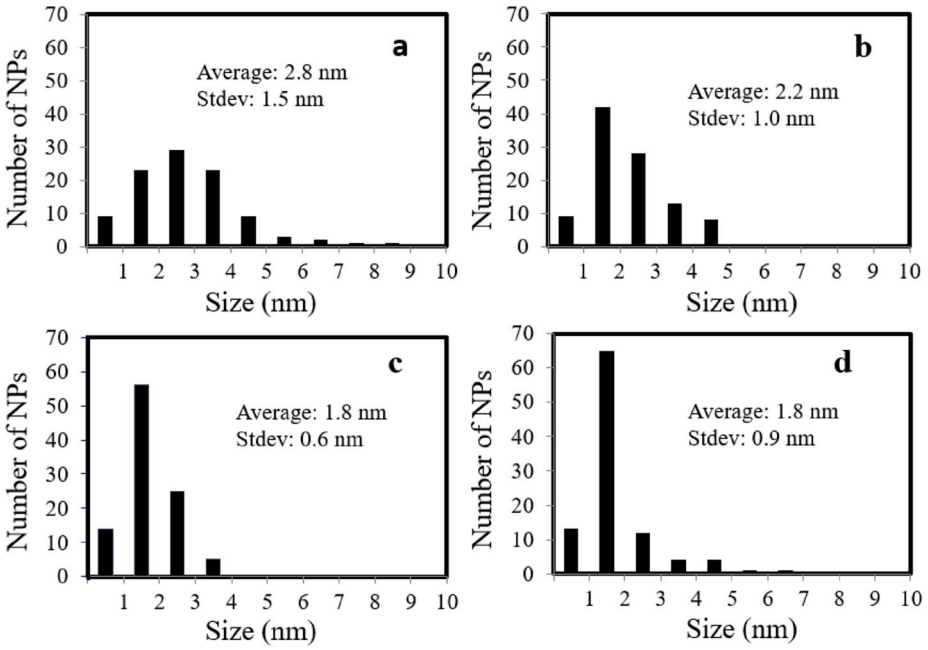

Fig. 3. Pt particle size versus number of particles distribution for (a) Oak Ridge's ORNL-2-002 sample, b) ORNL-023 sample, (c) EXO-0109 sample, and (d) EXO0308 sample.

the commercial Pt/GC (COM-Pt/GC) was conducted by the RDE voltage cycling AST between 0.1 V and 1.0 V. The ECSA and MA were recorded at both BOT and EOT stages and listed in Table 1. For the COM-Pt/GC sample, the ECSA dropped about 37% and MA dropped in 52% in upon 10,000 AST cycles. The two Pt-NbO_x/C catalysts as-made by ADP were undergone 25,000 cycles under the same AST. The APD-PN/GD-L lose 35% ECSA and 20% MA. The sample APD-PN/GC-b only lose about 6% ECSA and 20% MA. The STEM images of the sample APD-PN/GR-b displayed in Fig. 4b show that the Pt particle size is in the range of 2–4 nm. After 25,000 cycles AST the Pt particle grown up to 3–7 nm (Fig. 4c). It was caused by platinum dissolution and agglomeration during the AST test. In comparison, the commercial Pt/GC (COM-Pt/GC) sample, which is one of the state-of-art catalyst, the increase of its platinum particle size is more than 5 nm as shown in Fig. 4d BOT and Fig. 4e after EOT. These results clearly showed the greatly suppressed agglomeration and re-distribution of Pt nanoparticles of the APD-derived Pt-NbO_x catalysts in comparison to the commercial Pt/GC, indicative of their superior stability. For the PtNb/GC-b sample displayed in Fig. 4b, the Pt particle did not grow or agglomerate significantly, and most of the Pt particles were still anchored onto the NbO_x/C substrate. These results suggest that the NbO_x had a strong physical interaction with Pt, tightly holding Pt particles onto the substrate surface during the electrochemical cycling. The catalyst stability test also showed that NbO_x well mitigated catalysts performance loose in fuel cell

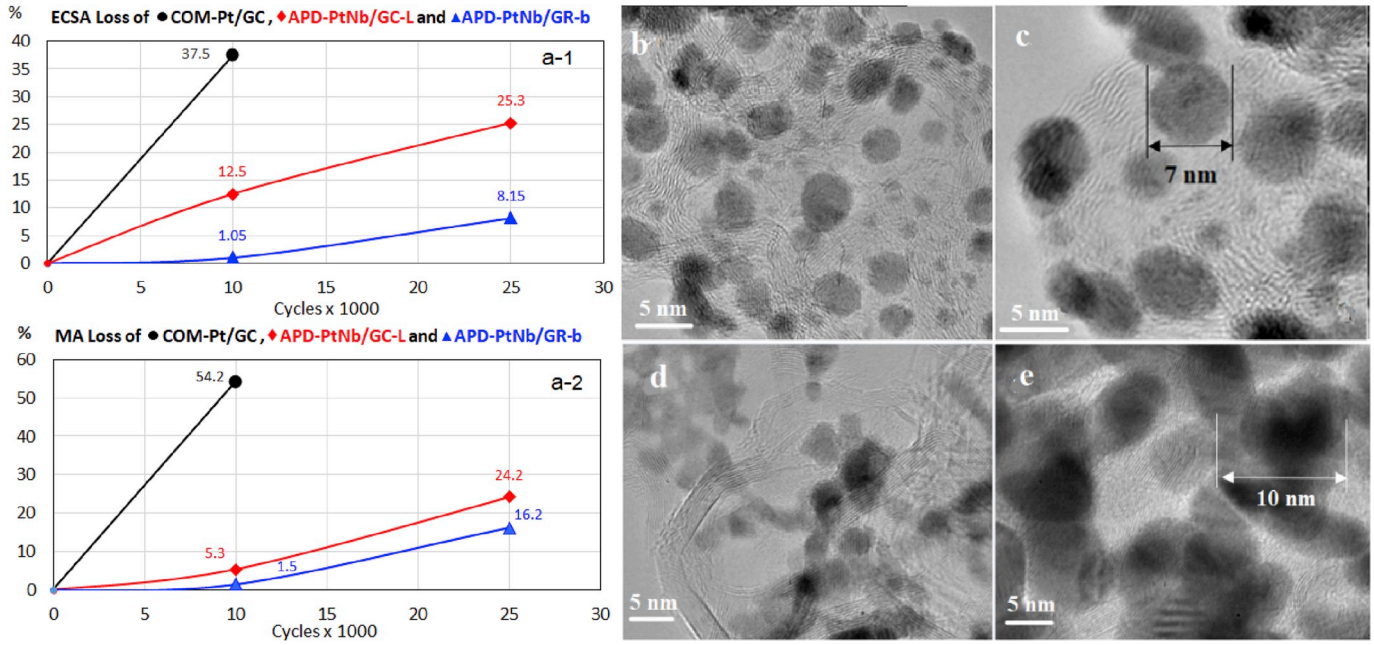

Fig. 4. a-1 & a-2) The catalyst's ECSA and MA loses under 0.1V–1.0V voltage cycling stability AST. b) A STEM image of the sample APD-PtNb/GC-b at BOT. c) The image of sample APD-PtNb/GC-b after 25,000 cycles AST. d) A STEM image of the COM-Pt/GC sample at BOT. e) The image of sample COM-Pt/GC after 10,000 cycles AST.

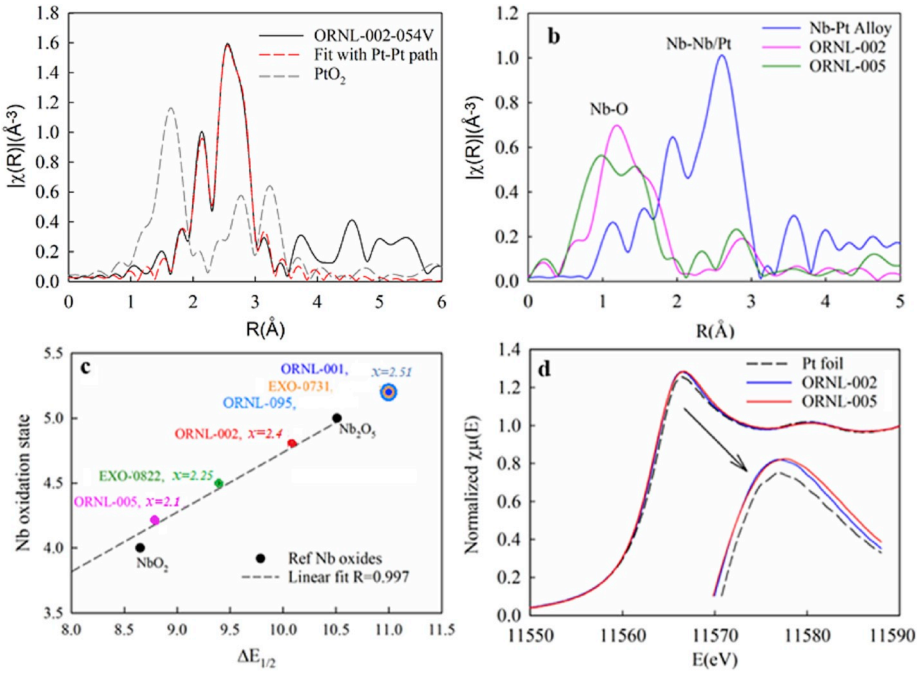

Fig. 5. (a) Pt L_3 FT-EXAFS and the corresponding fit spectrum; (b) Nb K-edge FT-EXAFS shows no Pt–Nb alloying phase, but prominent Nb–O interactions. (c) Nb oxidation state of tested samples as a function of their E_{edge}(s); the black dashed line is a guide to the eye. (d) The comparison of Pt L_3-edge spectrum of ORNL-002 and ORNL-005 to Pt foil collected at 0.54 V.

working conditions. It implied that NbO_x is more corrosion resistance than the graphitic carbon. NbO_x may slightly dissolve in fuel cell working conditions. Despite so, Nb^+ ion or NbO_x is not a Fengton agent which is not serious harmful to the fuel cell membrane.

3.2. *In situ* XAS characterization

EXAFS data were collected on PVD grown samples and are shown in Figs. 5 and 6. The *in situ* EXAFS analysis on ORNL samples indicates the lack of Pt–Nb interactions as shown in Fig. 5a and b from both the Pt and Nb perspectives. Specifically, the EXAFS of these two samples (ORNL-002 & −005) at the Pt L_3 edge can be well fitted with only a Pt–Pt path (Table 3), indicating the absence of Pt–Nb alloying effects. In the meantime, only Nb–O scattering peaks around 1.5 Å.

were observed on the Nb K-edge FT-EXAFS, and there is no Nb–Pt alloying phase which would give rise to a scattering peak between 2 and

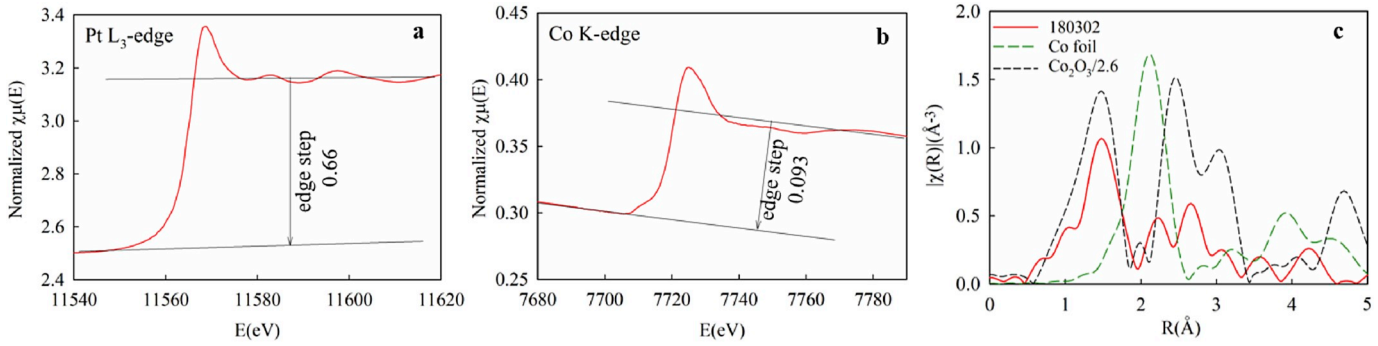

Fig. 6. a) Unnormalized XANES spectra of the Pt L_3 edge, b) The Co K-edge for Pt to Co ratio estimation. c) FT-EXAFS of the Co K-edge.

Table 3
Pt–Pt lattice distance and nearest neighbors.

Data at 0.54 V	$R_{Pt\text{-}Pt}$ (Å)	$N_{Pt\text{-}Pt}$
ORNL-002	2.756 ± 0.001	10.9 ± 0.4
ORNL-005	2.754 ± 0.001	10.0 ± 0.2
EXO-0302	2.740 ± 0.004	8.5 ± 0.8
Pt reference foil	2.766 ± 0.004	12

3 Å (Fig. 5b), further confirming the absence of Pt–Nb interaction. The Pt–Nb interactions was also absent in the Pt/NbO_x/C system prepared via the APD method; whereas the presence of Pt–O interactions wherein the O comes from the NbO_x, was observed [13]. Here the Pt–O scattering peak was not significant (Fig. 5a) likely because only a small fraction of Pt atoms on the surface interacts with the O. However, the Pt–O interactions in association with a partial electron transfer from Pt toward O is supported by the slightly higher white line intensity of the Pt XANES spectrum at 0.54 V (double-layer region) than that of the corresponding Pt reference foil, given that the white line intensity increases with increasing 5d orbital vacancies (Fig. 5d). The interactions between the supported metal and the oxygen in metal oxide support have been widely reported in metal supported on metal oxides systems, and ascribed to the possible cause for the strong metal and support interactions (SMSI) [11,13].

The oxidation states of the Nb in the studied samples were quantitatively evaluated from the edge position of the Nb XANES spectra in comparison to those of Nb-based baseline standards including Nb foil, NbO_2, and Nb_2O_5. This approach is justified by the fact that the oxidation state of Nb is linearly related to their E_{edge}, which is defined as the energy at which the normalized absorption of XANES is precisely one-half showed in Fig. 5c as reported by us [10]. The spectra show that the Nb in the ORNL-002 and ORNL-005 samples is slightly under saturated in terms of oxidation state (Fig. 5c). The oxidation state of Nb is between NbO2 and Nb2O5. Non-stoichiometric NbOx has higher electronic conductivity than saturated Nb2O5 [10], which is essential for the performance of PEMFCs. Nb oxidation state of the other 3 samples (ORNL-001, ORNL-095 and EXO-0731) were slightly higher than +5 (oversaturated). All three samples have relatively higher NbO_x loading and were synthesized by magnetron sputtering, which is different from the APD method, as reported in Ref. [12]. This discrepancy may have been caused by the oxygen to argon ratio in the processing gas when the target is Nb metal. Higher oxygen partial pressure will result in more oxidation of Nb. It is necessary to control the deposition conditions to keep the Nb oxidation state unsaturated to generate electronically conductive NbO_x, essential for the ORR activity and durability.

Pt is well known to bind oxygen ~0.2 eV too strong, and thus weakening the Pt–O bond improves the ORR activity of Pt. There are two routes to weaken the Pt–O bond, strain effect and ligand effect [31]. The Pt on NbO_x/C system enhances the ORR via the ligand effect caused by the Pt–O interaction, and/or the well-known beneficial strain effect in some circumstances [15–17]. Since shortened Pt–Pt bond length (strain effect) was not observed here, we deduced that the improved ORR activity of Pt is attributable to the ligand effect that arises from the Pt–O interaction wherein the O comes from the NbO_x. The O in NbO_x is in the oxidation of nearly −2 with the orbitals nearly fully filled by the electrons transferred from Nb. As a result, only trivial amounts of electrons can be transferred from Pt to the O to form the relatively weak Pt–O bonds. As a result, the Pt is only slightly d-electron deficient, which is confirmed by the slightly higher white line intensity of the Pt L_3 XANES spectra of Pt/NbO_x/C systems collected at 0.54 V compared to that of the Pt reference foil. Consequently, less electrons are transferred to the ORR intermediates such as OH_{ad}, leading to weakened Pt–O bond and improved ORR activity of Pt. Further improvements of the ORR activities can be realized by alloying the Pt with transition metal elements such as cobalt [32], therefore, PtCo alloy targets were used in Exothermics on amorphous carbon substrates (KB). *In situ* XAS on the NbO_x/C support PtCo alloy (EXO-0302) shows the presence of Pt–Co alloying phase as reflected by the shortened Pt–Pt distance (2.74 Å) compared to that of Pt foil (2.76 Å) (Table 3). This so-called strain effect downshifts the Pt d-band center relative to Fermi level which in turn weakens the Pt–O binding energy, hereby improving the ORR activity of Pt [33–35]. This means that the APD and magnetron sputtering synthesis processes are suitable to produce Pt-alloy catalysts onto the NbO_x/C substrate, and thus makes it possible to induce beneficial d-band interaction, strain and ligand effects simultaneously.

3.3. RDE results of ECSA and ORR activities

RDE data were systematically collected for screening performances of both APD and magnetron sputtering synthesized ORR catalysts. In our previous work [12], we reported RDE results of the 2.4 nm thick film Pt on NbO_x coated graphene. The Pt on this sample was magnetron sputtered onto a NbO_x functional layer, which was pre-coated onto a graphene (GR) layer that has been transferred onto a flat 5 mm diameter RDE glassy carbon (GLC) tip sample named Pt-FPN/GLC in Table 1. It exhibited the highest specific activity (2377 $\mu A cm^{-2}$) and high mass activity (495 $A g_{Pt}^{-1}$). The specific activity approaches that of the Pt bulk, which demonstrates the advantage of a 2D Pt nano-network structure on a substrate of NbO_x and GR for the ORR activities. The graphitized carbon (GC) with higher surface area compared to graphene powders was used in the APD process. Together with a non-stoichiometric NbO_x functional layer, GC can be used to improve Pt electrochemical effective surface area (ECSA). Graphene powders (GR) were also used in APD catalyst processing. A commercial ORR catalyst sample (COM-Pt/GC) with graphitized carbon nano-powder prepared via the conventional wet chemical method with about 47 wt% Pt loading was used for comparison. This commercial Pt/GC was used graphitized carbon which has better durability in comparison with other commercial wet-chemically processed nano-carbon supported Pt catalysts. In Table 1, the APD-prepared samples demonstrate higher ORR activities in

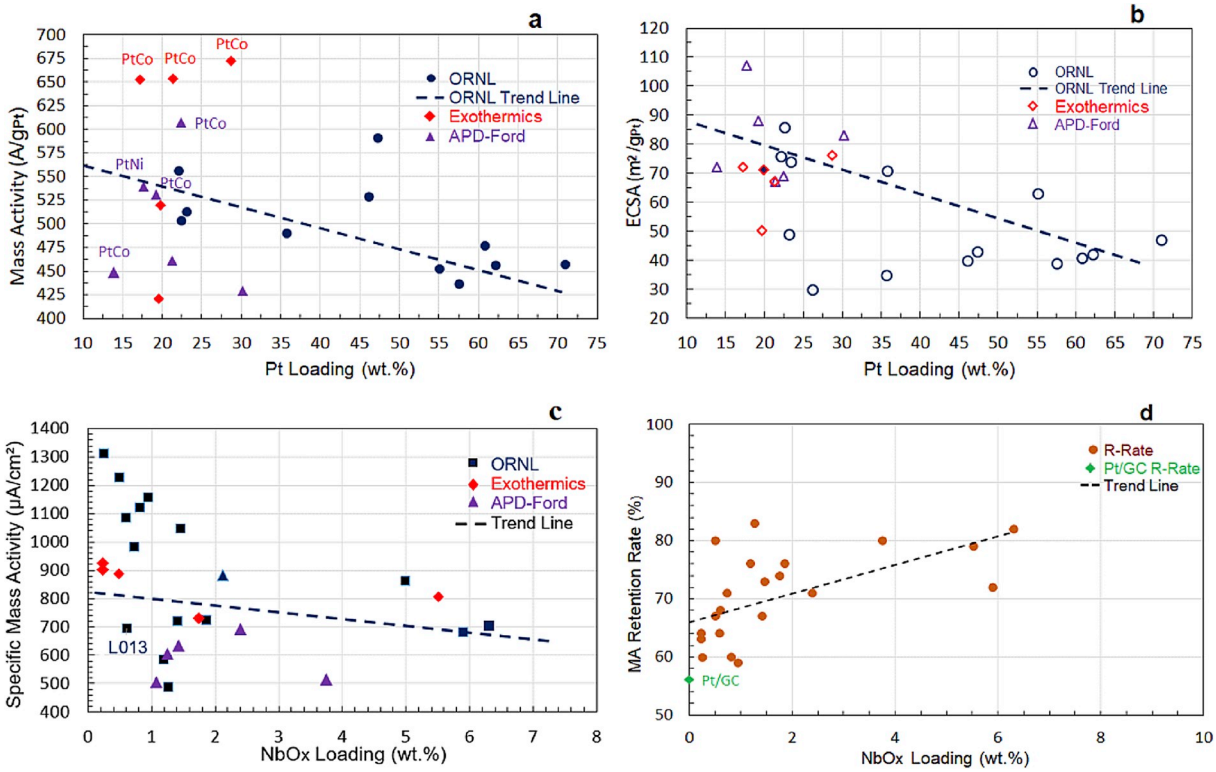

Fig. 7. RDE results summary: a) Mass activity versus Pt loading. b) Pt electrochemical surface area versus Pt loading. c) Catalyst specific mass activity versus NbO_x loading. d) Catalyst mass activity retention after voltage cycling versus NbO_x loading.

terms of both specific activities (SA) and mass activities (MA) albeit at lower Pt loadings. The samples APD-Pt/GC and APD-Pt/GR were produced by direct deposition of Pt on the GC and GR, respectively. Without the NbO_x functional layer, the specific and mass activities of the catalysts are higher than those of the baseline catalyst, but lower than those of the sample with the NbO_x functional layer. The graphitized carbon supported sample APD-PNb/GC-b with a 20 wt% Pt loading has twice the mass activity (309 Ag_{Pt}^{-1}) and a higher specific activity (566 μAcm^{-2}) versus the baseline COM-Pt/GC sample. The graphene supported APD-PN/GR catalyst with a 10 wt% Pt loading exhibits a high specific activity of 1003 μAcm^{-2}, and a mass activity of 345 Ag_{Pt}^{-1}. Reducing Pt loading to 5% on NbO_x/GR can further improve the specific and mass activity in the sample ADP-PN/GR-L. For this extremely low Pt loading sample, the APD process was used to alternatively deposit a layer of NbO_x followed by a layer of Pt for three cycles equally. The RDE test results in Table 1 show the beneficial effects of APD coated NbO_x incorporation as an intermediate layer on nano-carbon powder supports in improving the ORR activity.

A systematic study of the effect of carbon type, NbO_x concentration and Pt loading has been performed at ORNL, EXO and APD deposition methods, and the RDE results are summarized in Table 2. The MA of 23 magnetron sputtered and APD Pt (or Pt alloy) on NbO_x/C samples exceeded 400 Ag_{Pt}^{-1}. The analysis of RDE results of these samples are displayed in Fig. 7. The ORNL samples were intentionally made in wider range of Pt loading from 22.1 wt% to 71.0 wt%. In general, the BOT mass activity of ORNL (blue dots) samples decreases as Pt loading is increased (Fig. 7a). Five EXO samples have Pt loading between 17 wt% and 29 wt %. Three of them were made with targets of Pt alloyed with Co or Ni, corresponding to a molar composition close to ratio 3:1. The PtCo alloy samples showed higher activities. The mass activity advantage of PtCo and PtNi alloy was also shown in the three APD samples. From XAS results, Pt–Pt strain was created in these alloy samples that led to strain and ligand effects [24]. The mass activity can be further improved by tuning PtCo alloy composition to optimize the electron d-band structure of Pt and applying post treatment, such as acid leaching and annealing etc. In Fig. 7b, there is a trend of ECSA decreasing with increasing Pt loading, probably due to the Pt particles agglomeration on the carbon surface during magnetron sputtering or APD deposition as Pt weight percent increases. In terms of NbO_x loading effects, it can be seen that higher NbO_x loading did not significantly reduce the specific and mass activity of the catalysts (Fig. 7c). Furthermore, NbO_x could improve the electrocatalyst durability tremendously, as shown in Fig. 7d, where R-Rate represents the stability of the samples after completing the electrocatalyst AST. The trend guideline indicated that the samples with the higher NbO_x loading (up to 6.3 wt%) exhibited the higher retention rate, and that the commercial Pt/GC catalyst, ORNL-015 and ORNL-017 samples without NbO_x had much lower retention rate. These results indicate that NbO_x benefits durability. When comparing the catalysts with different types of carbon at similar NbO_x and Pt loading (ORNL-005 (GC), ORNL-022(AB) and EXO-0109(KB)), it can be seen that the performance is similar in terms of SA, MA and retention rate. Those results confirm that the morphology and distribution of NbO_x and Pt on the carbon nano-powders are more important than the type of carbon with respect to the ORR activities, ECSA and potential cycling. Detailed studies of the effects of the type of carbon on NbO_x and Pt morphology and support corrosion durability are still on-going. Several promising samples, such as ORNL-L013, ORNL-L031, EXO-0308, EXO-0302 and APD-0415 were chosen to be evaluated by MEA tests.

3.4. MEA test results

In early MEA tests [20], we focused on MEA evaluation of Ford APD Pt-NbO_x/C ORR catalysts. Cathode catalyst layers in the prior report were coated onto half-CCMs using a wire wound bar. In this work, the cathode catalyst layer was made using a Sono-Tek ultrasonic spray coating system. The performance of the MEA from Ford APD, ORNL and Exothermics with reasonable RDE results showed significant improvement compared to the prior report [20]. The 5 cm^2 MEA test results are

Table 4
5 cm^2 MEA's performance[a] for Ford APD, ORNL and Exothermics catalysts.

Sample	HFR ($m\Omega \cdot cm^2$)	MA ($A g_{Pt}^{-1}$)	ECSA ($m^2 g_{Pt}^{-1}$)	MA Retention Rate after 30K AST (%)
ORNL-L013	44	328	29	64
EXO-0109	53	123	30	69
EXO-0302	66	215	50	66
EXO-0308	49	306	36	70
APD-0110	49	288	17	68
APD-1106	48	270	39	67
COM-Pt/GC	50	141	38	54

[a] All MEA's tested with cathode I/C = 0.6, 0.10 mg/cm^2 Pt loading under 80 °C, 150 kPa, H_2/Air and 100% RH test conditions.

listed in Table 4. Because the as-made catalysts haven't undergone acid leaching and annealing post treatments, the catalysts may not possess the ideal morphology and structures which can limit the MEA performances.

The H_2/air polarization curves are shown in Fig. 8a. The H_2/air polarization has been measured on the commercial Pt/GC catalyst as well for comparison to the new catalysts as shown in Fig. 8b. Pt/GC has a low MA, as well as similar performance at higher current density as the newly developed catalysts, but relatively lower durability with retention rate of 54% MA and 25% ECSA, compared to the much higher values obtained on ORNL-013 and EXO-0308 as shown in Fig. 8c and d, respectively.

The durability was evaluated by the mass activity and ECSA retention rate after 30,000 cycles AST between 0.60 and 0.95 V. The MEA made from EXO-0308 showed a mass activity retention rate of 71% and an ECSA retention rate of 59%. The MEA made of ORNL-L013 showed a mass activity retention rate of 64% and an ECSA retention rate of 49%. The durability of both MEAs met the 60% mass activity retention rate target for 2025 using the AST [36].

4. Summary

A novel Pt on NbO_x/C catalytic system has been developed via PVD and APD methods. RDE results showed that the ECSA, ORR activities, and stability of this novel Pt on NbO_x/C catalyst system are higher than a commercial catalyst on graphitized carbon synthesized via conventional wet chemical methods. The non-stoichiometric NbO_x ($2 < x < 2.5$) is well stable in fuel cell working condition and the degree of oxygen incorporation plays an important role in the morphology and distribution of Pt on the catalyst. Pt shows remarkable high stability with NbO_x layers when subject to accelerated electrocatalyst stress test. As a metal oxide functional layer, NbO_x assists the catalyst ORR by improving the ORR activity of Pt via Pt–O interactions, and the induced strain effect, as well as the d-band interaction with alloying elements or substrates. Its unsaturated oxidation state assists electrical conductivity. Without the NbO_x functional layer, the Pt supported on graphitized carbon is unstable under the harsh ORR environment in PEMFCs. The MEA samples of ORNL and EXO have achieved in-cell mass activities of over 300 $A g_{Pt}^{-1}$. Future efforts will focus on PVD deposition conditions to control and optimize NbO_x and Pt loading to create a NbO_x templated Pt nanonetwork with uniform distribution on carbon substrate, and to maximize the NbO_x metal oxide functional layer conductivity so as to reach the DOE target [36] of the Pt mass activity of 440 $A g_{Pt}^{-1}$ in PEMFCs.

Declaration of competing interest

The authors declare that they have no known competing financial interests or personal relationships that could have appeared to influence the work reported in this paper.

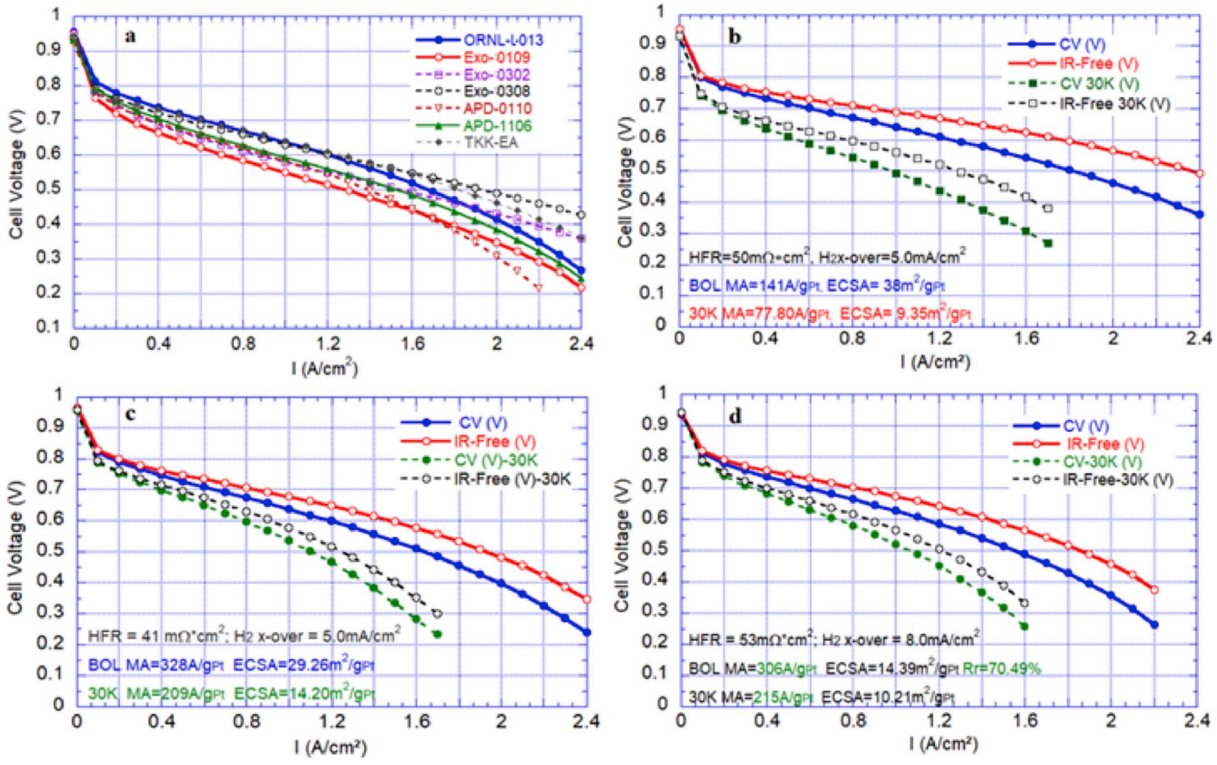

Fig. 8. a) 5 cm^2 MEA BOT H_2/air polarization curves of Ford APD, ORNL and Exothermics ORR catalysts. b) The commercial Pt/GC MEA's MA, ECSA and polarization curves before and after 30K Pt voltage cycles. c) The MA, ECSA and H_2/air polarization curves before and after 30K

Acknowledgement

This work was supported by Fuel Cell Technology Office under the Office of Energy Efficiency and Renewable Energy of the U.S. Department of Energy, through Contract No. DE-EE0007675. The authors gratefully acknowledge the use of Beamline 7-BM (QAS) and 8-ID (ISS) of the National Synchrotron Light Source (NSLS) II at Brookhaven National Laboratory, under U.S. DOE Contract No. DE-SC0012704. Thanks also extended to DOE project manager David Peterson.

Appendix A. Supplementary data

Supplementary data to this article can be found online at https://doi.org/10.1016/j.jpowsour.2020.227709.

References

[1] J. Chen, J. Hu, J.R. Waldecker, J. Electrochem. Soc. 162 (2015) F878–F889.
[2] H. Zhang, H. Haas, J. Hu, S. Kundu, M. Davis, C. Chuy, J. Electrochem. Soc. 160 (2013) F840–F847.
[3] F.T. Wagner, B. Lakshmanan, M.F. Mathias, J. Phys. Chem. Lett. 1 (2010) 2204–2219.
[4] S. Shahgaldi, J. Hamelin, Carbon 94 (2015) 705–728.
[5] P. Trogadas, T.F. Fuller, P. Strasser, Carbon 75 (2014) 5–42.
[6] Li Zhang, Liya Wang, Chris M.B. Holt, Titichai Navessin, Kourosh Malek, Michael H. Eikerling, David Mitlin, J. Phys. Chem. C 114 (2010) 16434–16474.
[7] Y. Wang, K.S. Chen, J. Mishler, S.C. Cho, X.C. Adroher, Appl. Energy 88 (2011) 981–1007.
[8] S. Huang, P. Ganesan, B.N. Popov, Appl. Catal. B Environ. 96 (2010) 224.
[9] C. Nico, T. Monteiro, M.P.F. Graça, Prog. Mater. Sci. 80 (2016) 1–37.
[10] R.F. Janninck, D.H. Whitmore, J. Chem. Phys. 37 (1962) 2750–2754.
[11] L. Zhang, L. Wang, C.M.B. Holt, T. Navessin, K. Malek, M.H. Eikerling, D. Mitlin, J. Phys. Chem. C 114 (2010), 16434.
[12] C. Xu, P. Pietrasz, J. Yang, R. Soltis, K. Sun, M. Sulek, R. Novak, ECS Trans. 58 (1) (2013) 1779–1788.
[13] Q. Jia, S. Ghoshal, J. Li, W. Liang, G. Meng, H. Che, S. Zhang, Z. Ma, S. Mukerjee, J. Am. Chem. Soc. 139 (2017) 7893–7903.
[14] G.M. Veith, A.R. Lupini, L. Baggetto, J.F. Browning, J.K. Keum, A. Villa, L. Prati, A. B. Papandrew, G.A. Goenaga, D.R. Mullins, S.E. Bullock, N.J. Dudney, Chem. Mater. 25 (2013) 4936–4945.
[15] G.M. Veith, A.R. Lupini, N.J. Dudney, J. Phys. Chem. C 113 (2009) 269–281.
[16] G.M. Veith, A.R. Lupini, S.J. Pennycook, N.J. Dudney, The use of magnetron sputtering for the production of heterogeneous catalysts, in: E. Gaigneaux, M. Devillers, D.E. De Vos, S. Hermans, P.A. Jacobs, J.A. Martens, P. Ruiz (Eds.), Studies in Surf. Sci. and Catalysis, vol. 162, Elsevier, Amsterdam, 2006, pp. 71–78.
[17] G.M. Veith, A.R. Lupini, S.J. Pennycook, G.W. Ownby, N.J. Dudney, J. Catal. 231 (2005) 151–158.
[18] G.M. Veith, A.R. Lupini, S.J. Pennycook, A. Villa, L. Prati, N.J. Dudney, Catal. Today 122 (2007) 248–253.
[19] G.M. Veith, A.R. Lupini, S.N. Rashkeev, S.J. Pennycook, D.R. Mullins, V. Schwartz, C.A. Bridges, N.J. Dudney, J. Catal. 262 (2009) 92–101.
[20] C. Xu, J. Yang, B.L. Pence, K. Gath, P. Pietrasz, M. Sulek, K. Sun, E. Sohm, G. Meng, ECS Trans. 64 (2014) 181–189.
[21] M. Newville, J. Synchrotron Radiat. 8 (2001) 322–324.
[22] B. Ravel, K. Gallagher, Phys. Scr. 2005 (2005) 606.
[23] M. Newville, P. Limacrvincedilscaron, Y. Yacoby, J.J. Rehr, E.A. Stern, Phys. Rev. B 47 (1993), 14126.
[24] A.L. Ankudinov, B. Ravel, J.J. Rehr, S.D. Conradson, Phys. Rev. B. 58 (1998) 7565–7576.
[25] M. Teliska, W.E. O'Grady, D.E. Ramaker, J. Phys. Chem. B 108 (2004) 2333–2344.
[26] Q. Jia, C.U. Segre, D. Ramaker, K. Caldwell, M. Trahan, S. Mukerjee, Electrochim. Acta 88 (2013) 604–613.
[27] Q. Jia, J. Li, K. Caldwell, D.E. Ramaker, J.M. Ziegelbauer, R.S. Kukreja, A. Kongkanand, S. Mukerjee, ACS Catal. 6 (2016) 928–938.
[28] Q. Jia, D.E. Ramaker, J.M. Ziegelbauer, N. Ramaswamy, A. Halder, S. Mukerjee, J. Phys. Chem. C 117 (2013) 4585–4596.
[29] H.A. Gasteiger, S.S. Kocha, B. Sompalli, T.F. Wagner, Appl. Catal., B 56 (2005) 9–35.
[30] M. Shao, A. Peles, K. Shoemaker, Nano. Lett. 11 (2011) 3714–3719.
[31] I.E.L. Stephens, A.S. Bondarenko, U. Grønbjerg, J. Rossmeisl, I. Chorkendorff, Energy Environ. Sci. 5 (2012) 6744, 31.
[32] Z. Xu, H. Zhang, H. Zhong, Q. Lu, Y. Wang, D. Su, Appl. Catal., B: Environ. 111–112 (2012) 264–270.
[33] V.R. Stamenkovic, B.S. Mun, M. Arenz, K.J.J. Mayrhofer, C.A. Lucas, G. Wang, P. N. Ross, N.M. Markovic, Nat. Mater. 6 (2007) 241–247.
[34] P. Strasser, S. Koh, T. Anniyev, J. Greeley, K. More, C. Yu, Z. Liu, S. Kaya, D. Nordlund, H. Ogasawara, M.F. Toney, A. Nilsson, Nat. Chem. 2 (2010) 454.
[35] Q. Jia, W. Liang, M.K. Bates, P. Mani, W. Lee, S. Mukerjee, ACS Nano 9 (2015) 1387.
[36] Fuel Cell Technical Team Roadmap Nov, US department of Energy, Fuel Cell Technologies Office, 2017. https://www.energy.gov/sites/prod/files/2017/11/f46/FCTT_Roadmap_Nov_2017_FINAL.pdf.